PHYSICAL REVIEW RESEARCH **7**, L022058 (2025)

Letter

Density-and-phase domain walls in a condensate with dynamical gauge potential

Sayak Bhattacharjee,[1,2,*,†] Roderich Moessner,[2] and Shovan Dutta[2,3]
[1]*Department of Physics, Indian Institute of Technology Kanpur, Kanpur 208016, India*
[2]*Max Planck Institute for the Physics of Complex Systems, Dresden 01187, Germany*
[3]*Raman Research Institute, Bengaluru 560080, India*

(Received 16 January 2023; accepted 5 May 2025; published 9 June 2025)

We show how one can generate domain walls that separate high- and low-density regions with opposite momenta in the ground state of a harmonically trapped Bose-Einstein condensate using a density-dependent gauge potential. Within a Gross-Pitaevskii framework, we elucidate the distinct roles of vector and scalar potentials and how they lead to synthetic electromagnetic fields that are localized at the domain wall. In particular, the kinetic energy cost of a steep density gradient is compensated by an electrostatic field that pushes particles away from a special value of density. We show numerically in one dimension that such a domain wall is more prominent for repulsive contact interactions, and becomes metastable at strong electric fields through a first-order phase transition that ends at a critical point as the field is reduced. We also provide simple variational *Ansätze* that reproduce this metastability. Our findings build on recent experimental developments and may be realized with cold atoms in a shaken optical lattice, providing insights into collective phenomena arising from dynamical gauge fields.

DOI: 10.1103/PhysRevResearch.7.L022058

Introduction. An important challenge facing engineered quantum systems is simulating the physics of gauge theories [1–3]. The goal is to probe phenomena such as confinement [4] as well as uncover new collective effects. A major advance was to realize artificial magnetic fields for neutral atoms and photons [5], which enabled, e.g., a realization of the Haldane model [6] and photonic Laughlin states [7]. Recent years have seen a coordinated effort to make such fields *dynamical* in order to probe interacting matter and gauge fields [8,9], as in quantum chromodynamics [10,11]. In particular, density-dependent gauge potentials, which play a key role in Chern-Simons physics [12], have been realized in Bose-Einstein condensates (BECs) by shaking [13,14] and Raman dressing [15,16]. These gauge fields do not have an independent degree of freedom but already produce intriguing domain walls in the experimental ground state [14], whose generation and dynamics are not well understood. Here, we elucidate how the emergent Lorentz forces allow one to stabilize and engineer a wider class of such domain walls.

Domain walls generally arise as topological defects in nonlinear media, which are of fundamental interest in magnetism [17,18] and astroparticle physics [19,20], and have applications in information processing [21] and optical communication [22]. In quantum-gas experiments, domain walls spontaneously excited in quenches provided an important test of Kibble-Zurek universality [23,24]. They are also created deterministically by shining light on parts of a condensate to imprint a phase, leading to dark solitons [25], or by applying a nonuniform magnetic field to a spinor condensate, which led to the observation of Dirac monopoles [26] and knot solitons [27] (see Ref. [28] for a review). A density-dependent gauge potential, on the other hand, allows one to shape the *ground-state* phase profile by coupling it to the local density [29]. This scheme was used by Yao *et al.* [14] to create phase domains in a harmonic trap, where the condensate switches between equal and opposite (canonical) momenta of a double well. However, the density profile itself was unaffected by the potential, i.e., no feedback was observed, limiting the range of accessible physics.

We show that the experimental scenario effectively corresponds to the case of a pure vector potential, for which the Lorentz forces vanish in a static condensate. Generically, applying a density-dependent tilt $\mathbf{A}(\rho)\cdot\mathbf{p}$ to the single-particle dispersion $\varepsilon(\mathbf{p})$, as in Ref. [14], yields both *electric* and vector potentials, which can be used to tailor density as well as phase variations. In particular, we show that instead of switching between opposite momenta, if one lets the single-particle ground state interpolate *smoothly* with density, e.g., by tilting a quadratic dispersion, then the electric potential can give rise to domain walls where the density falls sharply as the phase gradient reverses direction. We discuss a minimal model where such domain walls are tunable over a wide range of experimental parameters. Crucially, they represent ground-state topological structures where the synthetic electromagnetic fields are concentrated and may host previously unknown

---

[*] Contact author: sayakbhattacharjee@stanford.edu

[†] Present address: Department of Physics, Stanford University, Stanford, California 94305, USA.

collective modes. Furthermore, at sufficiently strong fields it can become energetically favorable to annihilate the domain wall through a first-order transition that ends at a critical point, which may be used to probe topological defect generation by false-vacuum decay relevant to inflationary cosmology [30].

Below, we first discuss the equations of motion within a Gross-Pitaevskii formalism before presenting numerical results and variational *Ansätze* for a one-dimensional (1D) model and discussing possible experimental realizations.

Synthetic Lorentz forces. The hydrodynamic equations of a BEC subject to a dynamical gauge potential were derived in Ref. [29]. Here, we explain how the resulting density-dependent electromagnetic forces shape the ground state. Note that the hydrodynamic form is equivalent to the Gross-Pitaevskii equation [31] and originates from the collective nature of a zero-temperature condensate, as opposed to collisional equilibration.

We consider identical bosons with quadratic dispersion and unit mass, i.e., $\varepsilon(\mathbf{p}) = |\mathbf{p}|^2/2$. A synthetic vector potential $\boldsymbol{\mathcal{A}}$ shifts the canonical momentum $\mathbf{p} \equiv -i\hbar\nabla$, rotating the phase of the wave function like a true vector potential acting on a unit charge. This shift results in the kinetic energy $\varepsilon_{\mathrm{kin}} = |\mathbf{p} - \boldsymbol{\mathcal{A}}|^2/2$, where $\mathbf{p} - \boldsymbol{\mathcal{A}}$ is the mechanical momentum. In shaking experiments a gauge potential may be realized by tilting the dispersion by $\boldsymbol{\mathcal{A}} \cdot \mathbf{p}$ [14]. However, this does not account for the $|\boldsymbol{\mathcal{A}}|^2$ term in $\varepsilon_{\mathrm{kin}}$. Stated differently, such a tilt is equivalent to a vector potential $\boldsymbol{\mathcal{A}}$ *and* a scalar potential $-|\boldsymbol{\mathcal{A}}|^2/2$. As we show below, these two play very separate roles in a static condensate, with important consequences.

To keep the discussion general, we consider a BEC with arbitrary density-dependent vector and scalar potentials $\boldsymbol{\mathcal{A}}(\rho)$ and $\mathcal{B}(\rho)$, respectively. Additionally, the particles are trapped in an external potential $V(\mathbf{r})$ and have pairwise s-wave contact interactions of strength g, which are both tunable in cold-atom setups [32]. At the mean-field level [31], the condensate is governed by the Hamiltonian

$$H = (1/2)|\mathbf{p} - \boldsymbol{\mathcal{A}}(\rho)|^2 + \mathcal{B}(\rho) + V(\mathbf{r}) + (g/2)\rho. \qquad (1)$$

The total energy is $\mathcal{E} = \langle\psi|H|\psi\rangle$, where $\psi(\mathbf{r}, t)$ is the condensate wave function varying in position $\mathbf{r}$ and time t. Writing $\psi = \sqrt{\rho}e^{i\varphi}$, where φ is the phase, we find

$$\mathcal{E} = \int d\mathbf{r}\left[\frac{\hbar^2}{2}\frac{|\nabla\rho|^2}{4\rho} + \frac{1}{2}\rho|\mathbf{v}|^2 + (\mathcal{B} + V)\rho + \frac{g}{2}\rho^2\right], \qquad (2)$$

where $\mathbf{v} := \hbar\nabla\varphi - \boldsymbol{\mathcal{A}}$ is the velocity of the condensate, and $\mathcal{B}(\rho) + V(\mathbf{r}) := \mathcal{V}(\rho, \mathbf{r})$ is the net scalar potential. In Eq. (2) the second term gives the classical kinetic energy and the first term describes a quantum correction, which vanishes for $\hbar \to 0$. The third and fourth terms represent potential and interaction energies, respectively.

The equation of motion can be obtained by minimizing the action $S = \int dt\langle\psi|i\hbar\partial_t - H|\psi\rangle$ [33] with respect to ρ and φ, with the constraint $\int d\mathbf{r}\rho(\mathbf{r}) = N$, where N is the total particle number. Using $\langle\psi|i\partial_t|\psi\rangle = -\int d\mathbf{r}\rho\partial_t\varphi$ and Eq. (2) gives the Euler-Lagrange equations

$$\partial_t\rho + \nabla\cdot\mathbf{j} = 0, \qquad (3a)$$

$$\hbar\partial_t\varphi + Q + |\mathbf{v}|^2/2 + \Phi + V + g\rho - \mu = 0, \qquad (3b)$$

where we have introduced a chemical potential μ as a Lagrange multiplier for the particle-number constraint, $\mathbf{j} := \rho\mathbf{v}$ is the current density, $Q := -(\hbar^2/2)(\nabla^2\sqrt{\rho}/\sqrt{\rho})$ is a quantum potential, and

$$\Phi := \partial_\rho(\rho\mathcal{B}) - \mathbf{j}\cdot\partial_\rho\boldsymbol{\mathcal{A}} \qquad (4)$$

is a potential resulting from the density-dependent fields. Equation (3a) is the continuity equation and Eq. (3b) is a quantum Hamilton-Jacobi equation [34], which differ from those of a standard condensate only by the presence of Φ. Note that when $\boldsymbol{\mathcal{A}}$ and $\mathcal{B}$ do not depend on ρ, $\Phi + V$ simply gives the net external potential $\mathcal{V}(\mathbf{r})$. To interpret Φ generally, we take the gradient of Eq. (3b) to find the Cauchy momentum equation

$$\frac{D\mathbf{v}}{Dt} = -\nabla(Q + V + g\rho) + \mathbf{E} + \mathbf{v}\times\mathbf{B}, \qquad (5)$$

where $D/Dt := \partial_t + \mathbf{v}\cdot\nabla$ is the convective or total time derivative for a fluid element, and

$$\mathbf{E} = -\nabla\Phi - \partial_t\boldsymbol{\mathcal{A}} \quad \text{and} \quad \mathbf{B} = -\nabla\times\mathbf{v} \qquad (6)$$

are the synthetic electric and magnetic fields, which encapsulate the effects of the density-dependent potentials. Thus, Φ acts as the electric potential. From Eq. (6) the magnetic field is set by the local vorticity and can be rewritten as $\mathbf{B} = \nabla\times\boldsymbol{\mathcal{A}} - \hbar\nabla\times\nabla\varphi$. The second term vanishes except where $\nabla\varphi$ is singular, e.g., at centers of quantized vortices [35]. Conversely, from Eqs. (4) and (6) the electric field is set by both ρ and $\mathbf{v}$.

Note that for $\mathcal{B} = 0$ the Lorentz forces vanish whenever the condensate is stationary. Thus, a nonzero scalar potential is *necessary* in order to modify the stationary density profiles, including that of any 1D ground state.

For such stationary states, $\mathbf{v} = 0$ implies $\nabla\varphi = \boldsymbol{\mathcal{A}}/\hbar$, i.e., the phase gradient is determined by the local vector potential, which was utilized in Ref. [14] to create phase domains. On the other hand, Eq. (3b) gives a generalized Gross-Pitaevskii equation (GPE) for the density,

$$Q[\rho] + \Phi_0[\rho] + V(\mathbf{r}) + g\rho = \mu - \hbar\omega, \qquad (7)$$

where ω is the rate of phase winding, which can be different for ground and excited states, and $\Phi_0 := \partial_\rho(\rho\mathcal{B})$ is the electrostatic potential, which does not depend on $\boldsymbol{\mathcal{A}}$. Hence, the roles of the vector and scalar potentials are uncoupled: $\mathcal{B}(\rho)$ changes the density variation caused by the trap, and $\boldsymbol{\mathcal{A}}(\rho)$ sets the phase profile.

To understand how the form of $\mathcal{B}$ affects the ground state in particular, note that in Eq. (2) it adds an energy per unit volume of $\rho\mathcal{B}(\rho)$, favoring more weight in values of density for which $\rho\mathcal{B}(\rho)$ is reduced. In particular, if the energy cost rises sharply around a special density ρ_c, the particles will be pushed away from ρ_c in both directions along the density axis by the electric field, which can give rise to domain walls separating high- and low-density regions, as we illustrate in the next section.

Model with domain wall. We focus on the case $\mathcal{B} = -|\boldsymbol{\mathcal{A}}|^2/2$ which is realized by applying only a tilt $\boldsymbol{\mathcal{A}}(\rho)\cdot\mathbf{p}$, as we explained in Sec. II. For this condition, the density and phase domains will coincide. However, this is not essential

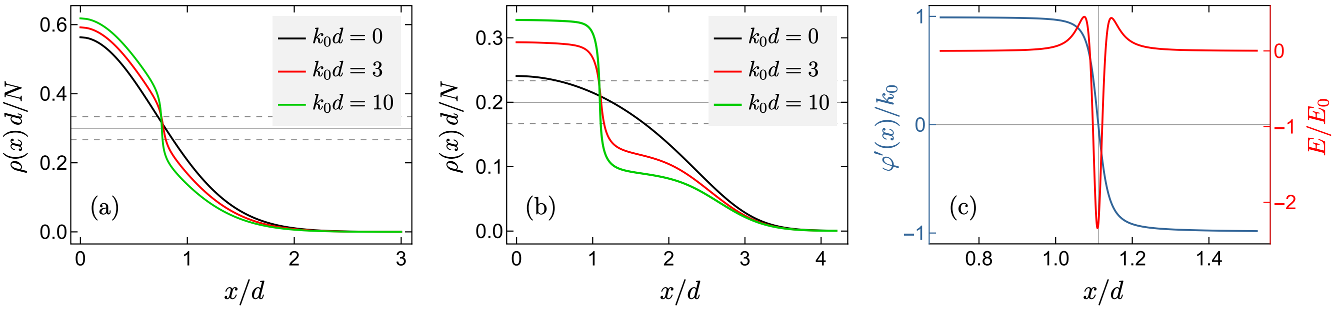

FIG. 1. (a), (b) Ground-state density profiles for $x > 0$ of a 1D BEC with N bosons in a harmonic trap of length d with interaction strength g in the presence of a density-dependent gauge potential given by Eq. (8) with $Nl/d = 30$ for (a) $\tilde{g} = 0$ and (b) $\tilde{g} = 40$, where $\tilde{g} := (2Nd/\hbar^2)g$ and $k_0 := p_0/\hbar$. The solid and dashed horizontal lines correspond to ρ_c and $\rho_c \pm 1/l$, respectively. As the gauge potential is increased, a steep slope emerges where $\rho = \rho_c$, becoming more prominent for stronger repulsive interactions. (c) Reversal of the phase gradient (dark blue) and a synthetic, localized electrostatic field [Eq. (6)] (red) for the $k_0d = 3$ curve in (b), where $E_0 := \hbar^2 k_0^3 Nl/d$. The vertical and horizontal lines show where $\rho = \rho_c$ and $\varphi' = 0$, respectively.

and more general profiles may be created by tuning $\boldsymbol{\mathcal{A}}$ and $\mathcal{B}$ separately.

Physical considerations. The simplest way to create a phase domain wall is by having $\boldsymbol{\mathcal{A}}(\rho)$ switch direction depending on whether the local density is above or below ρ_c, $\boldsymbol{\mathcal{A}} = p_0\,\mathrm{sign}(\rho - \rho_c)\hat{\mathbf{x}}$, where p_0 is the amplitude, $\hat{\mathbf{x}}$ is a unit vector, and sign(.) is the sign function. In the ground state $\boldsymbol{\nabla}\varphi$ follows $\boldsymbol{\mathcal{A}}$ to minimize the kinetic energy, i.e., the canonical momentum also changes sign where ρ crosses ρ_c [14]. However, this choice gives $\mathcal{B} = -p_0^2/2$, which is simply a constant and does not affect the density profile.

To produce a sharp fall in density, the crossover between $\pm p_0$ needs to occur over a finite density interval l^{-1}, as exemplified by

$$\boldsymbol{\mathcal{A}} = p_0 \tanh[(\rho - \rho_c)l]\hat{\mathbf{x}}. \tag{8}$$

Note that l has the dimension of volume, reducing to a length in 1D. Then, $\mathcal{B} = -(p_0^2/2)\tanh^2[(\rho - \rho_c)l]$ is peaked at ρ_c and penalizes densities in the range $\rho_\pm := \rho_c \pm 1/l$. For sufficiently large p_0 this effect can overcome the kinetic energy cost of steep density gradients [Eq. (2)] and stabilize a domain wall where ρ falls from ρ_+ to ρ_-. Concurrently, $\boldsymbol{\nabla}\varphi$ also changes direction across the domain wall [Eq. (8)], so the density and phase variations are correlated. For $l \to \infty$, $\boldsymbol{\mathcal{A}}$ goes back to the sign function, whereas for $l = 0$ the potentials vanish. Thus, a nonzero and finite value of l is necessary to see this physics.

Since $\boldsymbol{\mathcal{A}}$ and $\mathcal{B}$ vary appreciably only across the domain wall, the electromagnetic fields in Eq. (6) would also be concentrated there. This structure is reminiscent of flux-attached particles that give anyons in fractional quantum Hall physics [12,36,37]. Here also it is plausible that the domain walls will have interesting particle-like degrees of freedom, as suggested by first experiments [14].

The tanh form in Eq. (8) is by no means a prerequisite. In fact, in Appendix A we construct a family of smooth curves that approach a piecewise linear form of $\boldsymbol{\mathcal{A}}(\rho)$ and produce even sharper domain walls in 1D.

The density gradient at such a domain wall can be estimated for strong fields from a competition between the electrostatic and kinetic energies. For this purpose, we assume a domain wall of width w across which the density changes by $\Delta\rho \sim 2/l$. The domain wall has a surface area A and a volume wA. From Eq. (2) the electrostatic energy cost of having particles in this volume is $\mathcal{E}_{\mathrm{el}} \approx (p_0^2/2)\rho_c wA$. On the other hand, the kinetic energy cost of having a steep gradient of magnitude $s \approx \Delta\rho/w$ is $\mathcal{E}_{\mathrm{kin}} \approx (\hbar^2/2)[s^2/(4\rho_c)]wA$. Hence, the net energy cost, with $p_0 := \hbar k_0$, is

$$\mathcal{E}_{\mathrm{dw}} \approx \frac{\hbar^2}{2}A\Delta\rho\left(\frac{s}{4\rho_c} + \frac{k_0^2\rho_c}{s}\right), \tag{9}$$

which is minimized for $s = 2k_0\rho_c$. Including the interaction g gives a correction $\sim O(1/k_0)$ to s. This estimate agrees very well with numerical simulations in 1D (see Appendix B). Thus, whereas the density drop is set by l, the slope is set by $k_0\rho_c$ for sufficiently large k_0.

Numerical profiles. To reduce computational cost we explore ground states in 1D, where $\mathbf{v} = 0$, which already exhibit the salient features. Such 1D condensates have been realized in highly elongated traps [38] where the transverse motion is frozen out and the interaction g is renormalized [39]. We assume that the vector potential in Eq. (8) points along the longitudinal direction, which has a harmonic confinement of frequency ω. We take the trap length $d := \sqrt{\hbar/\omega}$ as our unit of length, and rescale the density by the particle number N, which gives the dimensionless parameters $\tilde{k}_0 := k_0 d$, $\tilde{\rho}_c := \rho_c d/N$, $\tilde{l} := Nl/d$, and $\tilde{g} := (2Nd/\hbar^2)g$. From Eq. (2) the rescaled energy functional is given by

$$\tilde{\mathcal{E}} = \int_{-\infty}^{\infty} \mathrm{d}\tilde{x}\left[\frac{(\partial_{\tilde{x}}\tilde{\rho})^2}{4\tilde{\rho}} + \tilde{\rho}\tilde{\mathcal{B}}(\tilde{\rho}) + \tilde{x}^2\tilde{\rho} + \frac{\tilde{g}}{2}\tilde{\rho}^2\right], \tag{10}$$

where $\tilde{\mathcal{E}} := 2\mathcal{E}/(N\hbar\omega)$, $\tilde{x} := x/d$, $\tilde{\mathcal{B}} := 2\mathcal{B}/(\hbar\omega)$, and the rescaled density $\tilde{\rho} := \rho d/N$ satisfies $\int \mathrm{d}\tilde{x}\tilde{\rho}(\tilde{x}) = 1$. We minimize $\tilde{\mathcal{E}}$ subject to this constraint, using an adaptive grid to accurately resolve the domain walls.

Figure 1(a) shows the density profiles for $g = 0$. When the scalar potential $\mathcal{B}$ is absent this is simply the Gaussian ground state of a harmonic trap. As k_0 is increased, a steep slope develops where ρ crosses ρ_c, signifying the domain wall. This becomes much more prominent if one turns on repulsive contact interactions, $g > 0$ [Fig. 1(b)]. As seen from Eq. (10), such interactions penalize density fluctuations, favoring a uniform profile. For $k_0 = 0$ this effect competes with the trap and

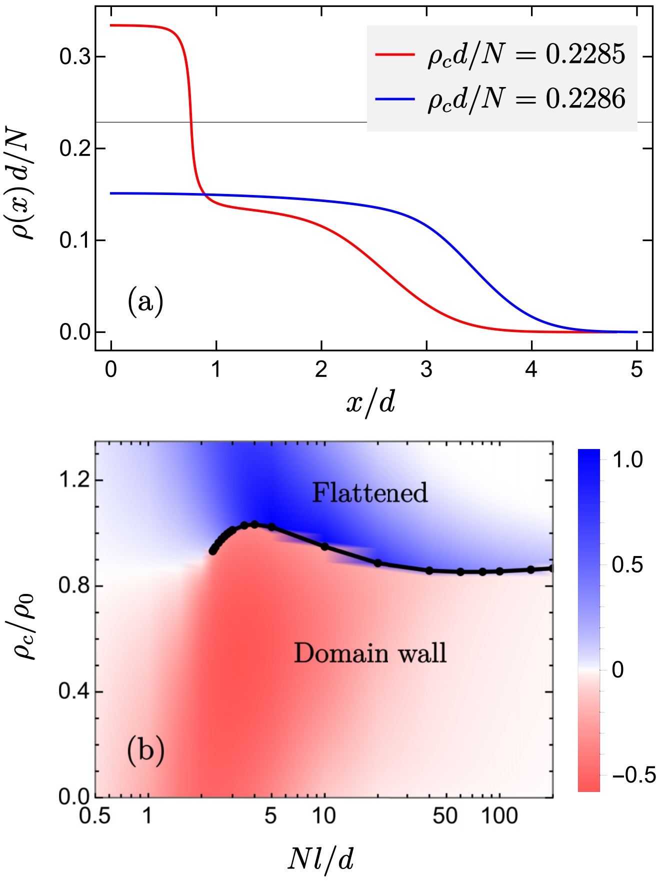

FIG. 2. (a) Discontinuous transition in the ground-state density for $\tilde{g} = 40$, $Nl/d = 30$, and $k_0 d = 5$. As ρ_c crosses above the transition point (horizontal line), it becomes energetically favorable to annihilate the domain structure (red) and create a flatter profile (blue) below ρ_c. (b) Phase diagram for $\tilde{g} = 10$ and $k_0 d = 2$, where ρ_0 is the peak density for $k_0 = 0$. The phase boundary (black curve) ends at a critical point for small l where the electric field is weak. The color tracks the potential energy difference, $\mathcal{E}_{\text{pot}}/\mathcal{E}_{0,\text{pot}} - 1$, where $\mathcal{E}_{0,\text{pot}}$ is the potential energy for $k_0 = 0$, showing one approaches the unperturbed ground state for $l \to 0$ and $l \to \infty$.

leads to a parabolic Thomas-Fermi profile for $\tilde{g} \gg 1$. On the other hand, when a domain wall is established by large k_0 the effect of g is to flatten the density on both sides of the wall, producing a wedding-cake-like structure.

Figure 1(c) shows how the phase reverses slope and the synthetic electric field is strongly localized at such a domain wall, as we argued previously. From Eqs. (4) and (6) the maximum value of the electric field scales as $k_0^3 l$. Note that there is no magnetic field in 1D.

Discontinuous phase transition. Creating a domain wall is one way to save electrostatic energy by removing particles from the range $\rho \sim \rho_c \pm 1/l$. Another way is to push the density everywhere below $\rho_c - 1/l$ [see Fig. 2(a)]. Such a state also lowers kinetic energy as it is flatter. However, it has high potential energy, as the cloud extends much farther from the center of the trap. This is particularly costly for $\rho_c \ll \rho_0$, where ρ_0 is the peak density without the gauge potential. Thus, for small ρ_c a domain wall is energetically favorable. However, as ρ_c is increased beyond ρ_0 the flatter state has to become the ground state. For sufficiently strong electric fields the two states are always separated by an energy barrier, at least in the Gross-Pitaevskii formalism, which results in a discontinuous phase transition as shown in Fig. 2(b). As one crosses the transition curve, the ground state changes dramatically [Fig. 2(a)] and the domain wall becomes metastable.

The decay of such a metastable state or "false vacuum" through quantum fluctuations plays a key role in models of the early universe [30], and experimental efforts are underway to probe this physics with quantum simulators [40,41]. The metastable lifetime depends on the energy barrier, which in our model can be tuned continuously by the gauge potential. In fact, as the electric field is reduced by decreasing l, we find the energy barrier shrinks to zero as the transition curve ends at a critical point [Fig. 2(b)]. For smaller values of l the two states are described by the same energy minimum and are no longer distinguishable. This structure is similar to the liquid-gas phase transition of water. At the critical point, the ground-state observables (e.g., the central density) vary infinitely fast with the system parameters (see Appendix C), as in a continuous phase transition.

Note that for $l \to 0$ or $l \to \infty$ the scalar potential $\mathcal{B}$ becomes insignificant and the ground state approaches that of the unperturbed system, as seen in Fig. 2(b).

Variational Ansätze. The ground states for both noninteracting and Thomas-Fermi limits can be reproduced by simple variational *Ansätze*, as detailed in Appendixes D and E. Below, we discuss the Thomas-Fermi limit for a piecewise linear potential $\mathcal{A}(\rho)$ that varies from p_0 to $-p_0$ between $\rho_c \pm 1/l$.

The *Ansatz* for the domain-wall solution is motivated by the numerical profiles in Figs. 1(b) and 3(a), which show a domain wall around ρ_c superimposed on a Thomas-Fermi background. We approximate the domain wall as a line segment of finite slope s, centered at some position x_d, which joins a Thomas-Fermi profile via constant-density plateaus at $\rho_c \pm 1/l$. This gives the following *Ansatz* (for $x \geqslant 0$) with s and x_d as the variational parameters:

$$\rho_{\text{dw}}(x) := \begin{cases} g^{-1}(\mu - x^2) & \text{if } x \leqslant x_l \\ \rho_c + 1/l & \text{if } x_l \leqslant x \leqslant x_- \\ \rho_c + s(x_d - x) & \text{if } x_- \leqslant x \leqslant x_+ \\ \rho_c - 1/l & \text{if } x_+ \leqslant x \leqslant x_r \\ g^{-1}(\mu - x^2) & \text{if } x_r \leqslant x \leqslant \sqrt{\mu} \end{cases}. \tag{11}$$

Here, the boundaries x_l, x_r, and $x_\pm$ are determined from continuity and μ is set by normalization.

On the other hand, the *Ansatz* for the flattened solution [Figs. 2(a) and 3(b)] has a central plateau at $\rho_c - 1/l$ which joins with a Thomas-Fermi wing at $x_b = \sqrt{\mu - g(\rho_c - 1/l)}$. This profile is entirely determined by normalization.

Figure 3 shows that the *Ansätze* agree well with exact numerics at strong fields and predict a transition at $\rho_c \approx \rho_0$ for $\tilde{l} \gg 1$, as in Fig. 2(b). However, at weak fields they do not reproduce the critical point, but give a transition at $\rho_c \gtrsim 1/l$. This is an artifact of requiring a density jump of $2/l$ in the domain-wall *Ansatz* and a peak density of $\rho_c - 1/l \geqslant 0$ in the flat *Ansatz*, which cease to hold for small l. Instead, the numerical profiles penetrate the field region and approach the zero-field solution, producing a critical point at $\rho_c \approx \rho_0$ and

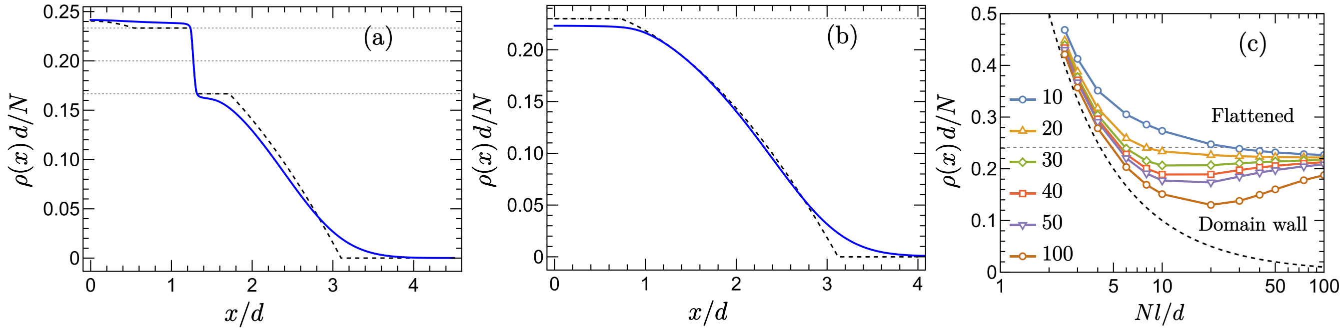

FIG. 3. (a), (b) Comparison of the ground-state profiles from exact numerics (solid curve) and the Thomas-Fermi variational *Ansätze* (see text; dashed curve) for a piecewise linear gauge potential [Eq. (A1) with $\eta = 16$] for $\tilde{g} = 40$ with (a) $\rho_c d/N = 0.2$, $k_0 d = 3$, $Nl/d = 30$, and (b) $\rho_c d/N = 0.28$, $Nl/d = 20$. Horizontal lines show $\rho = \rho_c$, $\rho_c \pm 1/l$ in (a) and $\rho = \rho_c - 1/l$ in (b). (c) Phase boundaries from the variational *Ansätze* for $\tilde{g} = 40$, which approach $\rho_c = 1/l$ (dashed curve) for small l and large k_0.

$l \sim 1/\rho_0$. In Appendix D we discuss more general *Ansätze* to capture this weak-field behavior.

Experimental realization. The key physical ingredient in our setup is that the minimum of the single-particle dispersion varies from $-k_0$ to $+k_0$ as the local density changes over a finite interval where the domain wall would appear. For this purpose we assumed a quadratic dispersion and a tilt that is a nonlinear function of density, saturating at $\pm k_0$ [e.g., as in Eq. (8)]. Such a nonlinear dependence may be hard to realize in experiments. However, one can circumvent the problem by turning on a lattice in the x direction, where the quasimomentum has a natural cutoff given by the Brillouin zone boundary, which could act as k_0. Then one requires only a linear tilt $\boldsymbol{\mathcal{A}} = A_0(\rho - \rho_c)\hat{\mathbf{x}}$, where A_0 controls the strength of the synthetic electrostatic field. This linear tilt was already implemented in Ref. [14] by shaking an optical lattice and oscillating the interaction strength $g(t)$ synchronously with the micromotion; depending on whether the occupation of a quasimomentum is in or out of phase with g, it gains or loses an average energy in the stroboscopic Hamiltonian. As g can be varied over a wide range through a Feshbach resonance [42], it is plausible that one can realize a sharp domain wall in density as well as probe its metastability and hysteresis across the discontinuous phase transition.

Summary and outlook. We have shown that a matter-dependent gauge potential can give rise to domain walls in a BEC with localized electromagnetic fields. In particular, we point out the necessity of a scalar potential for a sharp density gradient. Such a domain wall may be realized with cold atoms in a shaken lattice where one can probe its metastability across a tunable first-order phase transition.

Our findings motivate several open questions for future studies. First, how does one understand the dynamics of the domain walls? Already for the usual GPE, solitonic excitations exhibit rich dynamics [28]. What new degrees of freedom are introduced by the localized electromagnetic fields? How do velocity-dependent electric forces [Eq. (4)] and the associated lack of immediate Galilean invariance [43] manifest themselves in the dynamics? Does the domain wall behave like a particle with a negative charge-to-mass ratio, as suggested experimentally [14]? Further, what additional structures emerge in higher dimensions? This is particularly appealing because, starting in two dimensions, a BEC can have vortices in the ground state [44–46] and density-dependent magnetic forces [Eq. (5)], which add more nonlinearity to the problem and may alter the stability of the domain walls [47]. Answering these fundamental questions will be crucial to develop our understanding of collective structures arising from coupled matter and gauge fields.

Acknowledgments. S.B. gratefully acknowledges the Max Planck Summer Internship Fellowship 2022 for support during his stay at MPIPKS, where the work was carried out. This work was in part supported by the Deutsche Forschungsgemeinschaft under grant cluster of excellence ct.qmat (EXC 2147, Project No. 390858490).

Appendix A: Other forms of the gauge potential. Our predictions for the domain wall do not rely on the tanh variation of the gauge potential [Eq. (8)]. To illustrate this point we consider a different set of vector potentials $\boldsymbol{\mathcal{A}} = \hbar k_0 f_\eta[(\rho - \rho_c)l]\hat{\mathbf{x}}$, where

$$f_\eta(u) := \frac{1}{2\eta} \ln\left[\frac{\cosh(\eta(1+u))}{\cosh(\eta(1-u))}\right]. \tag{A1}$$

These functions are motivated by requiring their slope to reproduce the unit box function for $\eta \to \infty$, $f'_\eta(u) = (1/2)[\tanh(\eta(u+1)) - \tanh(\eta(u-1))]$. Thus, for $\eta \lesssim 1$, $f_\eta(u)$ is a smooth ramp, whereas for $\eta \gg 1$ it assumes a piecewise linear form, as shown in Fig. 4(a). Figure 4(b) shows that as η is increased the domain wall becomes more clearly confined between $\rho = \rho_c \pm 1/l$ while its slope $\rho'(x)$ is unaltered. From Eq. (7) the curvature $\rho''(x)$ at an edge of the domain wall is limited by $k_0^2 l \rho_c^2$.

Appendix B: Density gradient at the domain wall. In Fig. 5 we plot the numerically obtained density gradient at the domain wall for the profiles in Figs. 1(a) and 1(b). As the gauge potential increases, the slope converges to our estimate from the domain wall energy.

Appendix C: Variation across the phase transition. Figure 6 shows how ground-state observables change across the phase transition in Fig. 2(b). As the smoothness parameter l is decreased, a discontinuous jump turns into an infinite slope at the critical point, and subsequently becomes a crossover.

Appendix D: Thomas-Fermi Ansatz. In this Appendix, we provide exact expressions for the normalization condition and the energy functional corresponding to the *Ansätze* discussed

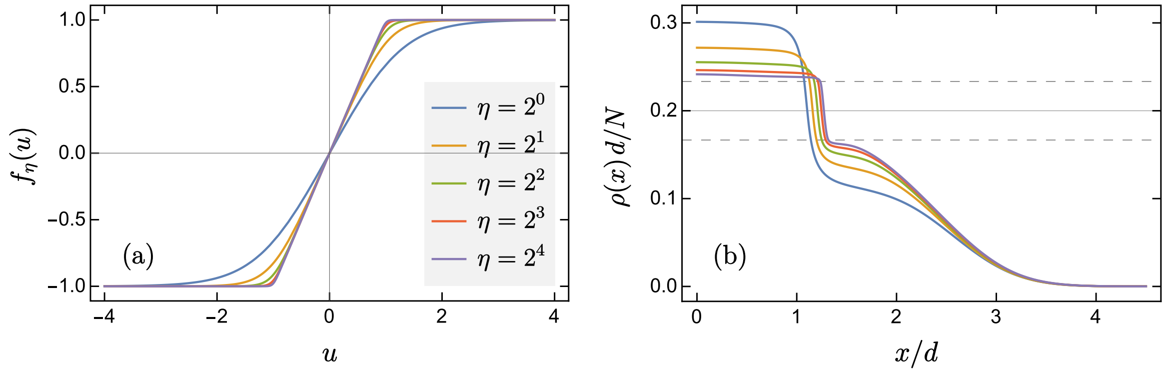

FIG. 4. (a) One-parameter family of curves that yield a piecewise linear variation of the gauge potential for $\eta \to \infty$. (b) Resulting ground-state density profiles for $\tilde{g} = 40$, $Nl/d = 30$, $k_0 d = 3$, and $\rho_c d/N = 0.2$ (solid horizontal line), corresponding to the red curve in Fig. 1(b), with the same color convention as in (a). As $\boldsymbol{\mathcal{A}}(\rho)$ becomes sharper the domain wall gets more pronounced between $\rho_c \pm 1/l$ (dashed horizontal lines).

in the main text. We use the rescaled variables (but denoted without the tilde accents).

We discuss the domain wall *Ansatz* in Eq. (11) first. The energy, a function of x_d, s, and μ, can be decomposed as follows:

$$\mathcal{E} = \mathcal{E}_{\text{kin}} + \mathcal{E}_{\text{field}} + \mathcal{E}_{\text{trap}} + \mathcal{E}_{\text{int}}$$

$$\mathcal{E}_{\text{kin}} = 2\int_0^\infty \mathrm{d}x\, \frac{(\partial_x \rho)^2}{4\rho}; \quad \mathcal{E}_{\text{field}} = 2\int_0^\infty \mathrm{d}x\, \rho\mathcal{B}(\rho);$$

$$\mathcal{E}_{\text{trap}} = 2\int_0^\infty \mathrm{d}x\, x^2\rho; \quad \mathcal{E}_{\text{int}} = 2\int_0^\infty \mathrm{d}x\, \frac{g}{2}\rho^2, \tag{D1}$$

which are the kinetic, scalar potential, trap, and interaction energy respectively. The kinetic energy can be ignored for the Thomas-Fermi profiles and is zero for the plateaux; thus, this contribution only comes from the domain wall.

The scalar potential comes from the piecewise linear vector potential and is given by

$$\mathcal{B}(\rho) = -\frac{k_0^2}{2}\begin{cases} 1 & \text{if } |\rho - \rho_c| \geqslant 1/l \\ l^2(\rho - \rho_c)^2 & \text{if } |\rho - \rho_c| < 1/l \end{cases} \tag{D2}$$

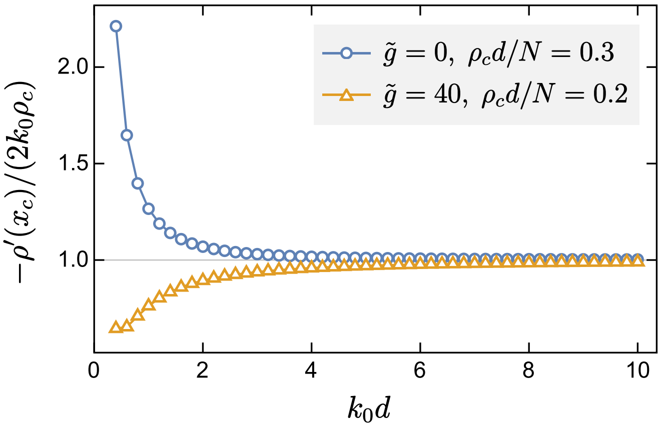

FIG. 5. Slope at the domain wall location x_c, where $\rho(x_c) := \rho_c$, for $Nl/d = 30$, corresponding to Figs. 1(a) (blue) and 1(b) (orange). In both cases $\rho'(x_c)$ approaches $-2k_0\rho_c$ at large k_0, in accordance with our estimate from Eq. (9).

We find it convenient to choose a shifted form of the scalar potential that does not affect our results—we choose $\mathcal{B}(\rho) \mapsto \mathcal{B}(\rho) + \frac{k_0^2}{2}$. This is nonzero only in the domain wall region.

The energies are given by

$$\mathcal{E}_{\text{kin}} = \frac{1}{2} s \ln\left(\frac{\rho_c + 1/l}{\rho_c - 1/l}\right), \tag{D3}$$

$$\mathcal{E}_{\text{field}} = k_0^2 \frac{4\rho_c}{3ls}, \tag{D4}$$

$$\begin{aligned}\mathcal{E}_{\text{trap}} = {} & \frac{2}{15g}\big(-3x_l^5 + 5x_l^3\mu\big) + \frac{2}{3}(\rho_c + 1/l)\big(x_-^3 - x_l^3\big) \\ & + \frac{4}{3}\frac{\rho_c + sx_d(3l^2 s x_d \rho_c - 2)}{(sl)^3} + \frac{2}{3}(\rho_c - 1/l)\big(x_r^3 - x_+^3\big) \\ & + \frac{2}{15g}\big(3x_r^5 - 5x_r^3\mu + 2\mu^{\frac{5}{2}}\big),\end{aligned} \tag{D5}$$

$$\begin{aligned}\mathcal{E}_{\text{int}} = {} & \frac{1}{15g}\big(3x_l^5 - 10x_l^2\mu + 15\mu^2\big) + g(\rho_c + 1/l)^2(x_- - x_l) \\ & + g\frac{6l^2\rho_c^2 + 2}{3l^3 s} + g(\rho_c - 1/l)^2(x_r - x_+) \\ & + \frac{1}{15g}\big(-3x_r^5 + 10x_r^3\mu - 15x_r\mu^2 + 8\mu^{\frac{5}{2}}\big).\end{aligned} \tag{D6}$$

The normalization condition can be written as an expression for the domain wall position x_d as the following three equivalent expressions:

$$\begin{aligned}x_d & = \frac{l}{3g}\left[x_r^3 - \big(x_r^2 - 2g\big)^{\frac{3}{2}} - \big(x_r^2 + g(\rho_c - 1/l)\big)^{\frac{3}{2}} + \frac{3g}{4}\right] \\ & = \frac{l}{3g}\left[x_r^3 - x_l^3 - \big(x_r^2 + g(\rho_c - 1/l)\big)^{\frac{3}{2}} + \frac{3g}{4}\right] \\ & = \frac{l}{3g}\left[\big(x_l^2 + 2g\big)^{\frac{3}{2}} - x_l^3 - \big(x_l^2 + g(\rho_c + 1/l)\big)^{\frac{3}{2}} + \frac{3g}{4}\right].\end{aligned} \tag{D7}$$

We note that the full solution is valid only for a subset of the parameter regime discussed in the phase diagram in Fig. 2(c). In particular, this solution is valid when $\rho_c l > 1$ and $\rho_c < \mu/g - 1/l$. As ρ_c is increased (at fixed l), ρ_c grows quicker than μ in a way that ρ_c becomes greater than $\mu/g - 1/l$.

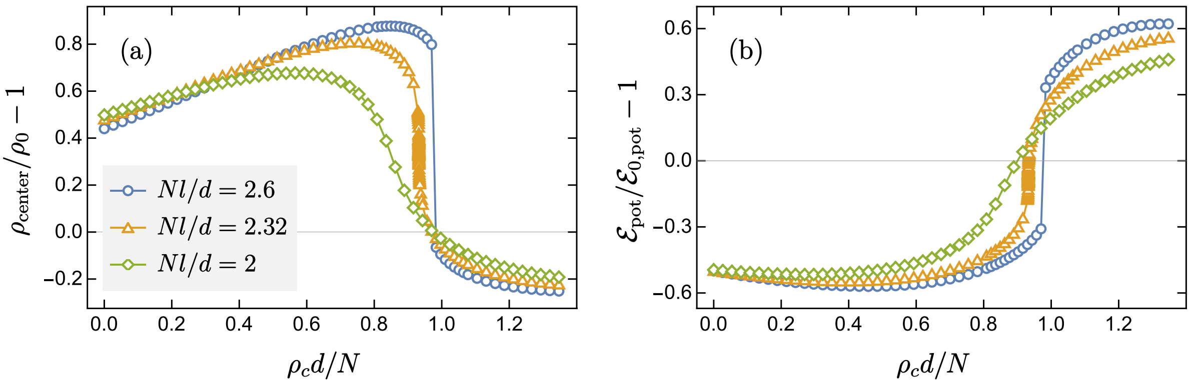

FIG. 6. Variation of the (a) peak density and (b) potential energy, measured relative to the unperturbed ground state, across the phase diagram for $\tilde{g} = 10$ and $k_0 d = 2$ shown in Fig. 2(b). The observables exhibit an infinite slope at the critical point l_c (orange), a jump across a first-order transition for $l > l_c$ (blue), and a smooth crossover for $l < l_c$ (green).

Then, the central Thomas-Fermi domain gets removed and the energy functional expressions in Eqs. (D5) and (D6) have to be changed—the correct expressions can be obtained by setting the first term and x_l equal to 0. Next, as ρ_c is further increased (at the same fixed l), there comes a point when $x_d < 1/(sl)$ and the plateau at $\rho_c + 1/l$ vanishes; however, we find that for our investigated parameter regimes, the phase transition always occurs before this point.

The flattened *Ansatz*, defined below for $x \geqslant 0$, has a central plateau at $\rho_c - 1/l$ until it meets the Thomas-Fermi profile at $\pm x_b$.

$$\rho_{\text{flat}}(x) := \begin{cases} \rho_c - 1/l & \text{if } 0 \leqslant x \leqslant x_b \\ g^{-1}(\mu - x^2) & \text{if } x_b \leqslant x \leqslant \sqrt{\mu} \\ 0 & \text{if } x \geqslant \sqrt{\mu} \end{cases} \tag{D8}$$

Here, $x_b = \sqrt{\mu - g(\rho_c - 1/l)}$ and is fixed by normalization—it is the positive real root of

$$x_b^3 - \left(x_b^2 + g(\rho_c - 1/l)\right)^{\frac{3}{2}} + 3g/4 = 0. \tag{D9}$$

The energy can be decomposed into the trap and interaction energy, since the scalar potential is absent below $\rho_c - 1/l$ and the kinetic energy is zero in the plateau and negligible for the Thomas-Fermi solution. In this case, we find

$$\mathcal{E} = \mathcal{E}_{\text{trap}} + \mathcal{E}_{\text{int}}, \tag{D10}$$

$$\mathcal{E}_{\text{trap}} = \frac{2}{3}(\rho_c - 1/l)x_b^3 + \frac{2}{15g}\left(3x_b^5 - 5x_b^3\mu + 2\mu^{\frac{5}{2}}\right), \tag{D11}$$

$$\begin{aligned} \mathcal{E}_{\text{int}} &= g(\rho_c - 1/l)^2 x_b \\ &\quad + \frac{1}{15g}\left(-3x_b^5 + 10x_b^3\mu - 15x_b\mu^2 + 8\mu^{\frac{5}{2}}\right), \end{aligned} \tag{D12}$$

where x_b is given by the solution to Eq. (D9). Again, as ρ_c is increased (at fixed l), ρ_c becomes greater than $\mu/g + 1/l$. Then, the central plateau at $\rho_c - 1/l$ vanishes and the solution is the Thomas-Fermi inverted parabola given by $\rho(x) = (1/g)[(3g/4)^{2/3} - x^2]$ and has an energy given by $\mathcal{E} = 3(3g/4)^{2/3}/5$.

For $\rho_c l < 1$, the profile has a central Thomas-Fermi dome, a plateau at $\rho_c + 1/l$, and a domain wall that goes to zero density. The central domain may be absent if $\rho_c > \mu/g - 1/l$. The corresponding energy expressions can be obtained in a similar fashion as above, and we refrain from providing the exact expressions in this Appendix in favor of conciseness.

We finally point out that the fixed domain wall height at $2/l$ contributes to not finding a critical point for small l, where the domain wall solution and the flattened solution are the same. To allow for a critical point, one may adapt the domain wall *Ansatz* by keeping a variable domain wall height h, which leads to an additional variational parameter. The *Ansatz* can be given by

$$\rho_{\text{dw}}(x) := \begin{cases} g^{-1}(\mu - x^2) & \text{if } 0 \leqslant x \leqslant x_l \text{ or } x_r \leqslant x \leqslant \sqrt{\mu} \\ \rho_c + h/2 & \text{if } x_l \leqslant x \leqslant x_- \\ \rho_c + s(x_d - x) & \text{if } x_- \leqslant x \leqslant x_+ \\ \rho_c - h/2 & \text{if } x_+ \leqslant x \leqslant x_r \\ 0 & \text{if } x \geqslant \sqrt{\mu} \end{cases}, \tag{D13}$$

where $x_l = \sqrt{\mu - g(\rho_c + h/2)}$ and $x_r = \sqrt{\mu - g(\rho_c - h/2)}$. We leave investigating the phase diagram with such an *Ansatz* for future work.

Appendix E: Noninteracting Ansatz. In this Appendix, we discuss the noninteracting *Ansätze* that approximate the numerically obtained ground states. As in the Thomas-Fermi limit, we expect the piecewise linear vector potential opens a domain wall at ρ_c on top of the noninteracting zero-field ground state. From our numerical solutions, we find that there is no plateau at $\rho_c \pm 1/l$ (unlike the Thomas-Fermi limit) and the domain wall of slope s can be directly joined with the rest of the solution.

The normalized ground state is given by the Gaussian, $\rho(x) = (1/\sqrt{\pi})e^{-x^2}$. The GPE given by

$$-\frac{\partial x^2 \sqrt{\rho}}{\sqrt{\rho}} + x^2 = \mu \tag{E1}$$

has the general solution

$$\sqrt{\rho(x)} = c_1 D_{\nu_1}(\sqrt{2}x) + c_2\, D_{\nu_2}(\mathrm{i}\sqrt{2}x), \tag{E2}$$

where $\nu_1 = \frac{1}{2}(\mu - 1)$, $\nu_2 = -\frac{1}{2}(\mu + 1)$, $D_\nu(x)$ is the parabolic cylinder function with parameter ν, and c_1 and c_2 are real coefficients, which can be determined by normalization and the properties of a physical wave function. We thus propose that the *Ansatz* in the region $x \geqslant 0$ is given by

$$\rho_{\mathrm{dw}}(x) = \begin{cases} (\rho_c + 1/l)\left(\frac{D_\nu(\sqrt{2}x)+D_\nu(-\sqrt{2}x)}{D_\nu(\sqrt{2}x_-)+D_\nu(-\sqrt{2}x_-)}\right)^2 & \text{if } x \leqslant x_- \\ \rho_c + s(x_d - x) & \text{if } x_- \leqslant x \leqslant x_+ , \\ (\rho_c - 1/l)\left(\frac{D_\nu(\sqrt{2}x)}{D_\nu(\sqrt{2}x_+)}\right)^2 & \text{if } x \geqslant x_+ \end{cases} \tag{E3}$$

where $x_\pm = x_d \pm 1/(sl)$ denote the extent of the domain wall. This *Ansatz* has three variational parameters as in the Thomas-Fermi limit—x_d, s, and ν, where ν is related to the chemical potential.

Using the form of the parabolic cylinder function for x near zero and ∞, we can approximate the *Ansatz* by the following simpler expression in terms of the product of Gaussians and polynomials:

$$\rho_{\mathrm{dw}}(x) \approx \begin{cases} (\rho_c + 1/l)e^{(1+2\nu)(x_-^2 - x^2)} & \text{if } x \leqslant x_- \\ \rho_c + s(x_d - x) & \text{if } x_- \leqslant x \leqslant x_+ . \\ (\rho_c - 1/l)e^{x_+^2 - x^2}\left(\frac{x}{x_+}\right)^{2\nu} & \text{if } x \geqslant x_+ \end{cases} \tag{E4}$$

We can now compute the energy functional exactly. For the domain wall solution, the energy can be decomposed as follows:

$$\mathcal{E} = \mathcal{E}_{\mathrm{kin}} + \mathcal{E}_{\mathrm{field}} + \mathcal{E}_{\mathrm{trap}}, \quad \mathcal{E}_{\mathrm{kin}} = 2\int_0^\infty \mathrm{d}x\, \frac{(\partial_x \rho)^2}{4\rho};$$

$$\mathcal{E}_{\mathrm{field}} = 2\int_0^\infty \mathrm{d}x\, \rho \mathcal{B}(\rho); \quad \mathcal{E}_{\mathrm{trap}} = 2\int_0^\infty \mathrm{d}x\, x^2 \rho. \tag{E5}$$

The kinetic energy now contributes in the entire region, as does the trap energy, while the scalar potential only contributes in the domain wall region. We use the shifted scalar potential given by $\mathcal{B}(\rho) + k_0^2/2$, where $\mathcal{B}(\rho)$ is stated in Eq. (D2). The energy functional is found to be given by

$$\mathcal{E} = \mathcal{E}_{\mathrm{kin}} + \mathcal{E}_{\mathrm{field}} + \mathcal{E}_{\mathrm{trap}}, \tag{E6}$$

$$\begin{aligned} \mathcal{E}_{\mathrm{kin}} = {} & \frac{1}{2}(\rho_c + 1/l)(1+2\nu)\left(\frac{\sqrt{\pi}}{\sqrt{1+2\nu}} e^{(1+2\nu)x_-^2} \mathrm{erf}[\sqrt{1+2\nu}\, x_-] - 2x_-\right) + \frac{1}{2} s \ln\left(\frac{\rho_c + 1/l}{\rho_c - 1/l}\right) \\ & + (\rho_c - 1/l) x_+^{-2\nu} e^{x_+^2}\left[\nu^2 \Gamma\left(\nu - \frac{1}{2}; x_+^2\right) - 2\nu\Gamma\left(\nu + \frac{1}{2}; x_+^2\right) + \Gamma\left(\nu + \frac{3}{2}; x_+^2\right)\right], \end{aligned} \tag{E7}$$

$$\mathcal{E}_{\mathrm{field}} = k_0^2 \frac{4\rho_c}{3ls}, \tag{E8}$$

$$\begin{aligned} \mathcal{E}_{\mathrm{trap}} = {} & \frac{(\rho_c + 1/l)}{2(1+2\nu)}\left[\frac{\sqrt{\pi}}{\sqrt{1+2\nu}} e^{(1+2\nu)x_-^2} \mathrm{erf}[\sqrt{1+2\nu}\, x_-] - 2x_-\right] + \frac{4}{3}\frac{[\rho_c + s x_d (3l^2 s x_d \rho_c + 2)]}{(sl)^3} \\ & + (\rho_c - 1/l) e^{x_+^2} (x_+)^{-2\nu} \Gamma\left(\nu + \frac{3}{2}; x_+^2\right), \end{aligned} \tag{E9}$$

where $\mathrm{erf}\, z = \frac{2}{\sqrt{\pi}}\int_0^z \mathrm{d}t\, e^{-t^2}$ is the error function and $\Gamma(a; z) = \int_z^\infty t^{a-1} e^{-t}\, \mathrm{d}t$ is the incomplete Gamma function. The normalization condition is given by

$$(\rho_c + 1/l)e^{(1+2\nu)x_-^2} \frac{\sqrt{\pi}}{\sqrt{1+2\nu}} \mathrm{erf}[\sqrt{1+2\nu}\, x_-] + \frac{4\rho_c}{sl} + (\rho_c - 1/l)e^{x_+^2}(x_+)^{-2\nu}\Gamma\left(\nu + \frac{1}{2}; x_+^2\right) = 1. \tag{E10}$$

The *Ansatz* must be minimized with respect to x_d, s, and ν subject to this normalization condition.

The flattened solution *Ansatz* is a plateau at $\rho_c - 1/l$ up to $\pm x_b$ and which connects to the zero-field parabolic cylinder solution beyond that. For $x \geqslant 0$, we can write this as

$$\rho_{\mathrm{flat}}(x) := \begin{cases} \rho_c - 1/l & \text{if } 0 \leqslant x \leqslant x_b \\ (\rho_c - 1/l)\frac{D_\nu(\sqrt{2}x)}{D_\nu(\sqrt{2}x_b)} & \text{if } x_b \leqslant x \leqslant \sqrt{\mu} . \\ 0 & \text{if } x \geqslant \sqrt{\mu} \end{cases} \tag{E11}$$

We can approximate this as before, and write the *Ansatz* as

$$\rho_{\mathrm{flat}}(x) := \begin{cases} \rho_c - 1/l & \text{if } 0 \leqslant x \leqslant x_b \\ (\rho_c - 1/l)e^{x_b^2 - x^2}\left(\frac{x}{x_b}\right)^{2\nu} & \text{if } x \geqslant x_b . \end{cases} \tag{E12}$$

Here, the energy functional has a component from the kinetic energy and a trap energy. These are given by

$$\begin{aligned} \mathcal{E} & = \mathcal{E}_{\mathrm{kin}} + \mathcal{E}_{\mathrm{trap}}, \\ \mathcal{E}_{\mathrm{kin}} & = (\rho_c - 1/l)x_b^{-2\nu} e^{x_b^2}\left[\nu^2\Gamma\left(\nu - \frac{1}{2}; x_b^2\right) \right. \\ & \qquad \left. - 2\nu\Gamma\left(\nu + \frac{1}{2}; x_b^2\right) + \Gamma\left(\nu + \frac{3}{2}; x_b^2\right)\right], \\ \mathcal{E}_{\mathrm{trap}} & = \frac{2}{3}(\rho_c - 1/l)x_b^3 + (\rho_c - 1/l)e^{x_b^2}(x_b)^{-2\nu}\Gamma\left(\nu + \frac{3}{2}; x_b^2\right). \end{aligned} \tag{E13}$$

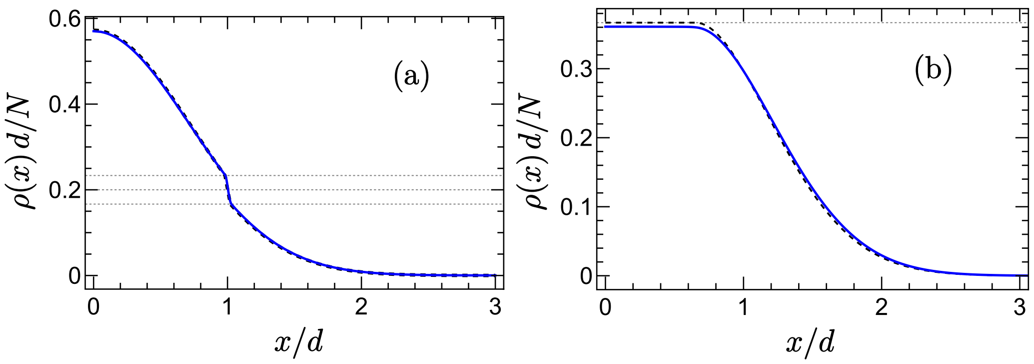

FIG. 7. Ground-state density profiles (blue) for $x > 0$ of a 1D BEC with N bosons in a harmonic trap of length d with no interactions in the presence of a piecewise linear density-dependent gauge potential [given by Eq. (A1) with $\eta = 16$] with $Nl/d = 30$ for (a) the domain wall solution at $\rho_c d/N = 0.2$ and $k_0 d = 5$ and (b) the flattened solution at $\rho_c d/N = 0.4$. The black dashed curves are the ground-state density profiles obtained from the variational *Ansätze* in Eqs. (E4) and (E12). The gray dashed lines in (a) are at $\tilde{\rho}_c$ and $\tilde{\rho}_c \pm 1/l$, while the dashed line in (b) is at $\tilde{\rho}_c - 1/l$.

This energy has two variational parameters x_b and ν. This must be minimized subject to the normalization condition given by

$$x_b + \frac{1}{2}e^{x_b^2}(x_b)^{-2\nu}\Gamma\left(\nu + \frac{1}{2}, x_b^2\right) = \frac{1}{2(\rho_c - 1/l)}. \quad \text{(E14)}$$

We compare the numerically obtained solutions with the variational solutions in Fig. 7 for the noninteracting limit and find great agreement—even better than the agreement in the Thomas-Fermi limit. We expect the phenomenology and the phase diagram in the noninteracting limit to be qualitatively similar to that of the Thomas-Fermi limit.

---

[1] E. Zohar, J. I. Cirac, and B. Reznik, Quantum simulations of lattice gauge theories using ultracold atoms in optical lattices, Rep. Prog. Phys. **79**, 014401 (2016).

[2] U.-J. Wiese, Ultracold quantum gases and lattice systems: quantum simulation of lattice gauge theories, Ann. Phys. **525**, 777 (2013).

[3] M. Dalmonte and S. Montangero, Lattice gauge theory simulations in the quantum information era, Contemp. Phys. **57**, 388 (2016).

[4] W. L. Tan, P. Becker, F. Liu, G. Pagano, K. S. Collins, A. De, L. Feng, H. B. Kaplan, A. Kyprianidis, R. Lundgren *et al.*, Domain-wall confinement and dynamics in a quantum simulator, Nat. Phys. **17**, 742 (2021).

[5] M. Aidelsburger, S. Nascimbene, and N. Goldman, Artificial gauge fields in materials and engineered systems, C. R. Physique **19**, 394 (2018).

[6] G. Jotzu, M. Messer, R. Desbuquois, M. Lebrat, T. Uehlinger, D. Greif, and T. Esslinger, Experimental realization of the topological haldane model with ultracold fermions, Nature (London) **515**, 237 (2014).

[7] L. W. Clark, N. Schine, C. Baum, N. Jia, and J. Simon, Observation of laughlin states made of light, Nature (London) **582**, 41 (2020).

[8] F. Görg, K. Sandholzer, J. Minguzzi, R. Desbuquois, M. Messer, and T. Esslinger, Realization of density-dependent Peierls phases to engineer quantized gauge fields coupled to ultracold matter, Nat. Phys. **15**, 1161 (2019).

[9] C. Schweizer, F. Grusdt, M. Berngruber, L. Barbiero, E. Demler, N. Goldman, I. Bloch, and M. Aidelsburger, Floquet approach to $\mathbb{Z}_2$ lattice gauge theories with ultracold atoms in optical lattices, Nat. Phys. **15**, 1168 (2019).

[10] U.-J. Wiese, Towards quantum simulating QCD, Nucl. Phys. A **931**, 246 (2014).

[11] M. C. Banuls, R. Blatt, J. Catani, A. Celi, J. I. Cirac, M. Dalmonte, L. Fallani, K. Jansen, M. Lewenstein, S. Montangero *et al.*, Simulating lattice gauge theories within quantum technologies, Eur. Phys. J. D **74**, 165 (2020).

[12] G. Valentí-Rojas, N. Westerberg, and P. Öhberg, Synthetic flux attachment, Phys. Rev. Res. **2**, 033453 (2020).

[13] L. W. Clark, B. M. Anderson, L. Feng, A. Gaj, K. Levin, and C. Chin, Observation of density-dependent gauge fields in a Bose-Einstein condensate based on micromotion control in a shaken two-dimensional lattice, Phys. Rev. Lett. **121**, 030402 (2018).

[14] K.-X. Yao, Z. Zhang, and C. Chin, Domain-wall dynamics in Bose–Einstein condensates with synthetic gauge fields, Nature (London) **602**, 68 (2022).

[15] M. J. Edmonds, M. Valiente, G. Juzeliūnas, L. Santos, and P. Öhberg, Simulating an interacting gauge theory with ultracold Bose gases, Phys. Rev. Lett. **110**, 085301 (2013).

[16] A. Frölian, C. S. Chisholm, E. Neri, C. R. Cabrera, R. Ramos, A. Celi, and L. Tarruell, Realizing a 1D topological gauge theory in an optically dressed BEC, Nature (London) **608**, 293 (2022).

[17] G. F. Nataf, M. Guennou, J. M. Gregg, D. Meier, J. Hlinka, E. K. H. Salje, and J. Kreisel, Domain-wall engineering and topological defects in ferroelectric and ferroelastic materials, Nat. Rev. Phys. **2**, 634 (2020).

[18] D. M. Evans, V. Garcia, D. Meier, and M. Bibes, Domains and domain walls in multiferroics, Phys. Sci. Rev. **5**, 20190067 (2020).

[19] A. Vilenkin and E. P. S. Shellard, *Cosmic Strings and Other Topological Defects* (Cambridge University, Cambridge, 1994).

[20] K. Saikawa, A review of gravitational waves from cosmic domain walls, Universe **3**, 40 (2017).

[21] G. Catalan, J. Seidel, R. Ramesh, and J. F. Scott, Domain wall nanoelectronics, Rev. Mod. Phys. **84**, 119 (2012).

[22] Y. Song, X. Shi, C. Wu, D. Tang, and H. Zhang, Recent progress of study on optical solitons in fiber lasers, Appl. Phys. Rev. **6**, 021313 (2019).

[23] L. W. Clark, L. Feng, and C. Chin, Universal space-time scaling symmetry in the dynamics of bosons across a quantum phase transition, Science **354**, 606 (2016).

[24] A. Keesling, A. Omran, H. Levine, H. Bernien, H. Pichler, S. Choi, R. Samajdar, S. Schwartz, P. Silvi, S. Sachdev *et al.*, Quantum Kibble–Zurek mechanism and critical dynamics on a programmable Rydberg simulator, Nature (London) **568**, 207 (2019).

[25] S. Burger, K. Bongs, S. Dettmer, W. Ertmer, K. Sengstock, A. Sanpera, G. V. Shlyapnikov, and M. Lewenstein, Dark solitons in Bose-Einstein condensates, Phys. Rev. Lett. **83**, 5198 (1999).

[26] M. W. Ray, E. Ruokokoski, S. Kandel, M. Möttönen, and D. S. Hall, Observation of Dirac monopoles in a synthetic magnetic field, Nature (London) **505**, 657 (2014).

[27] D. S. Hall, M. W. Ray, K. Tiurev, E. Ruokokoski, A. H. Gheorghe, and M. Möttönen, Tying quantum knots, Nat. Phys. **12**, 478 (2016).

[28] E. Kengne, W.-M. Liu, and B. A. Malomed, Spatiotemporal engineering of matter-wave solitons in Bose–Einstein condensates, Phys. Rep. **899**, 1 (2021).

[29] Y. Buggy, L. G. Phillips, and P. Öhberg, On the hydrodynamics of nonlinear gauge-coupled quantum fluids, Eur. Phys. J. D **74**, 92 (2020).

[30] S. Coleman, Fate of the false vacuum: Semiclassical theory, Phys. Rev. D **15**, 2929 (1977).

[31] C. J. Pethick and H. Smith, *Bose–Einstein Condensation in Dilute Gases* (Cambridge University, Cambridge, 2008).

[32] F. Schäfer, T. Fukuhara, S. Sugawa, Y. Takasu, and Y. Takahashi, Tools for quantum simulation with ultracold atoms in optical lattices, Nat. Rev. Phys. **2**, 411 (2020).

[33] P. Kramer and M. Saraceno, *Geometry of the Time-Dependent Variational Principle in Quantum Mechanics* (Springer-Verlag, Berlin, 1981).

[34] L. E. Ballentine, *Quantum Mechanics: A Modern Development* (World Scientific, Singapore, 2014), Chap. 14.

[35] A. L. Fetter and A. A. Svidzinsky, Vortices in a trapped dilute Bose-Einstein condensate, J. Phys.: Condens. Matter **13**, R135 (2001).

[36] Z. F. Ezawa, *Quantum Hall Effects: Field Theoretical Approach and Related Topics* (World Scientific, Singapore, 2008), Chap. 8.

[37] G. Valentí-Rojas, A. J. Baker, A. Celi, and P. Öhberg, Topological gauge fields and the composite particle duality, Phys. Rev. Res. **5**, 023128 (2023).

[38] A. Görlitz, J. M. Vogels, A. E. Leanhardt, C. Raman, T. L. Gustavson, J. R. Abo-Shaeer, A. P. Chikkatur, S. Gupta, S. Inouye, T. Rosenband *et al.*, Realization of Bose-Einstein condensates in lower dimensions, Phys. Rev. Lett. **87**, 130402 (2001).

[39] M. Olshanii, Atomic scattering in the presence of an external confinement and a gas of impenetrable bosons, Phys. Rev. Lett. **81**, 938 (1998).

[40] S. Abel and M. Spannowsky, Quantum-field-theoretic simulation platform for observing the fate of the false vacuum, PRX Quantum **2**, 010349 (2021).

[41] B. Song, S. Dutta, S. Bhave, J.-C. Yu, E. Carter, N. Cooper, and U. Schneider, Realizing discontinuous quantum phase transitions in a strongly correlated driven optical lattice, Nat. Phys. **18**, 259 (2022).

[42] C. Chin, R. Grimm, P. Julienne, and E. Tiesinga, Feshbach resonances in ultracold gases, Rev. Mod. Phys. **82**, 1225 (2010).

[43] Y. Buggy and P. Öhberg, Gauge transformations and Galilean covariance in nonlinear gauge-coupled quantum fluids, Phys. Rev. A **102**, 033342 (2020).

[44] Y.-J. Lin, R. L. Compton, K. Jiménez-García, J. V. Porto, and I. B. Spielman, Synthetic magnetic fields for ultracold neutral atoms, Nature (London) **462**, 628 (2009).

[45] S. Butera, M. Valiente, and P. Öhberg, Quantized vortices in interacting gauge theories, J. Phys. B: At., Mol. Opt. Phys. **49**, 015304 (2016).

[46] S. Butera, M. Valiente, and P. Öhberg, Vortex dynamics in superfluids governed by an interacting gauge theory, New J. Phys. **18**, 085001 (2016).

[47] B. A. Malomed, Vortex solitons: Old results and new perspectives, Physica D **399**, 108 (2019).